Computational Prediction of Broadband Noise from a Representative Small Unmanned Aerial System Rotor

Christopher S. Thurman
Graduate Research Assistant
University of Maryland
College Park, MD, USA

Nikolas S. Zawodny
Research Aerospace Engineer
NASA Langley Research Center
Hampton, VA, USA

James D. Baeder
Professor
University of Maryland
College Park, MD, USA

ABSTRACT

This work details the application of a lattice-Boltzmann method–very-large-eddy simulation (LBM-VLES) employed by the software suite, PowerFLOW. This LBM-VLES simulation predicted the aeroacoustic noise emanating from a representative, small unmanned aircraft system rotor, namely, the DJI-9450 in a hover condition. Predicted total aerodynamic loading as well as 2D aerodynamic loading along discrete spanwise sections of a rotor blade were compared to lower fidelity predictions and experimental results acquired in the Structural Acoustic Loads and Transmission anechoic chamber facility at the NASA Langley Research Center. The total acoustic spectra were decomposed into tonal and broadband components, which showed that broadband noise was a dominant contributor above 1 kHz for this rotor. These data were then compared to experimentally acquired data, showing good agreement up to approximately 11 kHz. Above 11 kHz, however, a grid sensitivity study showed dependency of the highest resolvable frequency on the spatial resolution of the computational domain, explaining the roll off in predicted data. Individual broadband noise sources were further investigated by calculating one-third octave sound pressure levels of the unsteady pressure fluctuations acting on the rotor, providing evidence that blade self-noise was the prominent noise source. Using these results, blade wake interaction noise was seen to be negligible for this particular rotor, which was further validated by calculating blade vortex miss distances and comparing to theory.

NOTATION

Ω	Rotor rotational rate, revolutions per minute (RPM)
$c_{0.75}$	Rotor chord length at 75% span, inches
R	Rotor tip radius, inches
C_p	Pressure coefficient, dimensionless
SPL	Sound pressure level, dB
$\bar{p}_{rms}$	Root mean square pressure, Pa
p_{ref}	Reference pressure, $20\mu Pa$
PSD	Power spectral density, dB/Hz
P_{xx}	Power spectral density, Pa^2/Hz
Δf	Narrowband spectra frequency resolution, Hz
θ	Observer angle relative to rotor plane, deg.

INTRODUCTION

Recent years have seen a considerable increase in the number of small unmanned aircraft systems (sUAS) in the US due to their potential for missions such as package delivery and aerial surveillance. Studies have shown that a large portion of the broadband noise emanating from typical sUAS vehicles lies in the most perceptive range of human audibility and can, at times, be more prevalent than tonal noise (Ref. 1). This, therefore, mandates a need for accurate prediction methodologies to better understand the noise generating mechanisms associated with sUAS broadband noise so that mitigation strategies may be implemented.

Semiempirical methods for broadband noise prediction have been developed in Refs. 2 and 3 and have been used to some degree of accuracy in Refs. 2 - 5. Though these methods provide valuable insight into the different broadband self-noise generating mechanisms, they lack the ability to capture more complex aerodynamically induced noise generation associated with rotorcraft such as atmospheric turbulence ingestion noise (TIN) and blade wake interaction (BWI) noise. This is due to these techniques having been developed based upon a wind tunnel campaign of various, fixed, 2D and 3D NACA0012 airfoil sections. These methods also entail the use of various empirical manipulations to account for different airfoil geometric characteristics, which may abate the accuracy of their predictions.

Higher fidelity approaches involving computational simulations have also been used to predict the aerodynamics and aeroacoustics of rotors associated with sUAS as well as with larger vehicles. The intent of these studies, however, was the total noise prediction, primarily focusing on tonal noise (Refs. 5 and 6). Methods to separate the broadband noise contributions from the total acoustic spectra have been developed in Ref. 5 and have been used on experimental results; however, these methods have not yet been used to post-process computational data.

Presented at the VFS International 76th Annual Forum & Technology Display, Virginia Beach, Virginia, USA, Oct. 6–8, 2020.
Copyright © 2020 by the Vertical Flight Society and United States Government as represented by the Administrator of the National Aeronautics and Space Administration. All rights reserved.

Due to the increasing relevance of broadband noise in the context of these smaller vehicles, there is a need for more direct and more accurate approaches to predict and isolate broadband noise so that it can be decomposed into its rudimentary aerodynamic foundations and studied in more detail.

The research detailed in this paper focuses on the accurate prediction and study of broadband noise emanating from a representative sUAS rotor, namely an isolated DJI Phantom 3 rotor (DJI-9450), using high-fidelity computational simulations.

TECHNICAL APPROACH

The computational strategy implemented in this work is comprised of first simulating the flowfield surrounding the rotor using a lattice-Boltzmann method–very-large-eddy simulation (LBM-VLES) solver, PowerFLOW. The rotor was then treated as an impermeable Ffowcs Williams-Hawkings (FW-H) surface and a forward-time solution (Ref. 7) of Farassat's formulation 1A (Ref. 8) was used to propagate acoustic pressures from the rotor surface to defined observers, which was done within the post-processing software suite, PowerACOUSTICS.

Aerodynamic loading results, as well as acoustic measurement data from experimental testing were readily availabe for comparison purposes and will be discussed in the Results section. These experiments were conducted in the Structural Acoustic Loads and Transmission (SALT) anechoic chamber facility at the NASA Langley Research Center (Ref. 9) using the same testing rig described in Ref. 5. Using these data and considering the DJI Phantom 3 gross vehicle weight of 2.68 lb, a representative hover case was selected, which produced 0.75 lb of thrust per rotor at $\Omega = 5100$ RPM.

Lattice-Boltzmann Methodology

The lattice-Boltzmann method (LBM) employed by the commercial software suite, PowerFLOW, was used to simulate the flowfield encompassing the DJI-9450 rotor due to its proven accuracy on similarly complex rotorcraft problems (Refs. 10 - 13). LBM is based on kinetic theory and uses a statistical description of discrete particle motion along 19 directions in three-dimensional space (D3Q19). LBM is explicit in nature, solving first for the convection of mesoscopic fluid particles before solving for the collision of these particles using the Bhatnagar-Gross-Krook model (Ref. 14). The reader is referred to Refs. 15 and 16 for a more detailed theoretical explanation of LBM.

Contrary to standard turbulence modeling procedures used by traditional Navier-Stokes solvers that use closure models to approximate the Reynolds stress as an effective eddy viscosity contribution to the governing equations, PowerFLOW uses a very-large-eddy simulation (VLES) to calculate a turbulent relaxation time based upon local turbulence parameters: strain, vorticity, and helicity (Ref. 10). The method for calculating this relaxation time is similar to that of traditional two equation turbulence closure models, but it is used to recalibrate

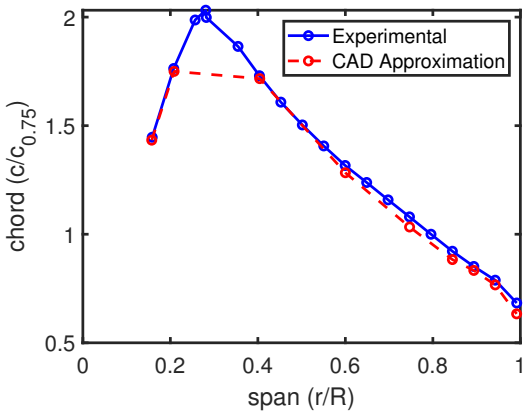

(a) Chord.

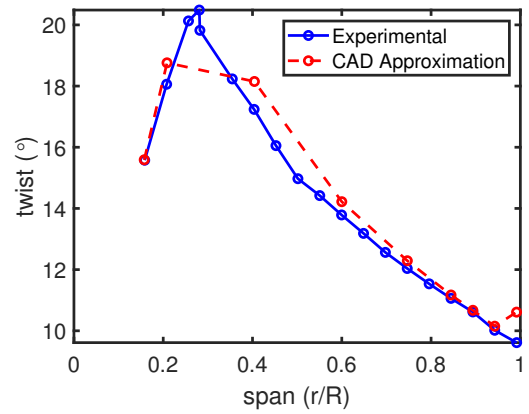

(b) Twist.

Figure 1: Comparison of GrabCAD DJI-9450 Rotor Geometry to Ref. 18.

the viscous relaxation time in the Boltzmann equation to the relevant time scales associated with turbulent motion. In this fashion, the unresolved, subgrid turbulence is realized by the governing equation.

In addition to modeling the subgrid turbulence, PowerFLOW uses a geometry cut-cell approach in conjunction with wall functions, which are extended to include the effects of pressure gradients, to generalize the near wall turbulence to that of the well known universal turbulence profile, The Law of the Wall (Ref. 17). This technique significantly reduces the computational cell count by eliminating the need for body fitted, stretched boundary layer grids like those commonly associated with traditional Navier-Stokes solvers.

Computational Setup

The rotor geometry was taken from the GrabCAD community website and was validated at different spanwise locations (Fig. 1) by comparing to measurements provided in Ref. 18. The span and chord in Fig. 1 were nondimensionalized with respect to the rotor span of 4.7 inches and the rotor chord at the 75% span, $c_{0.75}$, which was 0.645 inches.

A computational domain consisting of purely hexahedron cells, or voxels, surrounding the rotor and shown in Fig. 2,

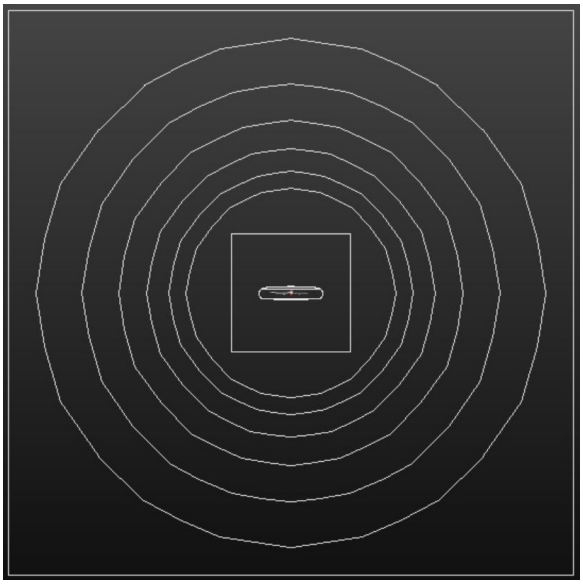

Figure 2: Full Computational Domain Visualization.

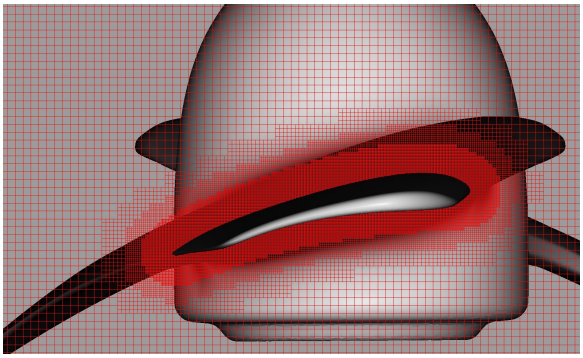

Figure 3: Nearfield Resolution Visualization along Rotor Blade.

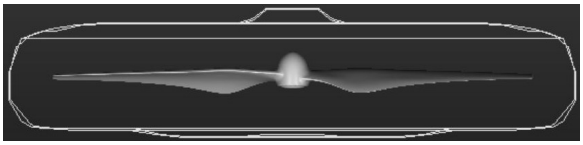

Figure 4: Rotational Volume Visualization.

was then created in PowerFLOW by first defining three very finely resolved regions, which offset the rotor. The first of which, had a cell length of 0.001843 inches ($c_{0.75}/350$). Each successive region moving outward from the rotor doubled the cell size of the former region, as seen in Fig. 3. Another region, shown in Fig. 4, was then defined as a rotational volume, encompassing the rotor and the finely resolved offset regions. This volume and all its constituents rotated at the same rotational rate as the rotor while the rest of the computational domain remained stationary. A stationary cylinder was defined outside of this rotational volume and spanned 10.5 inches in all directions (2.23R), which served to provide adequate resolution for capturing rotor wake and nearfield flow dynamics.

Table 1: Rotor Aerodynamic Loading Results.

Source	Thrust	Relative Error
Experimental	0.75 lb	
Fine Resolution	0.6241 lb	16.79%
Medium Resolution	0.5973 lb	20.36%
Coarse Resolution	0.5736 lb	23.52%

A series of spheres were defined around this wake region to gradually decrease the resolution until the farfield, which was 50 inches away from the rotor on all sides (10.64R).

The computational domain consisted of 565 million voxels and a time step of 7.05E-08 seconds was internally calculated by PowerFLOW using a Courant-Friedrichs-Lewy (CFL) number of 1 and given the aforementioned simulation parameters of the finest voxel size. A CFL number of 1 was maintained for the temporal update of each voxel throughout the computational domain, meaning that a voxel in a given resolution region updated twice as often as a voxel in an adjacent region of finer resolution. With this in mind, there were a total of 133 million 'fine equivalent' voxels, which greatly reduced the computation time (2.32E+05 CPU hours).

A no-slip boundary condition was imposed on the rotor surface and ambient standard temperature and pressure (STP) conditions, as well as a zero velocity condition, were imposed on the outer boundaries of the computational domain for the hover case. Turbulent wall functions were used in the first voxel adjacent to the rotor geometry to approximate the boundary layer up to y+ distances of 3.08 and 7.99 for the spanwise locations of maximum chord length and the reference chord location, 28% and 75% span, respectively.

AERODYNAMIC RESULTS

The PowerFLOW simulation was conducted over 13 rotor revolutions with the last 6 being used to record unsteady surface pressures on the rotor at a sampling rate of 80 kHz. Convergence of the aerodynamic flowfield had been determined to occur at the 7th revolution. A grid refinement study was performed in which the grid resolution was sequentially coarsened by a factor of $\sqrt{(2)}$ for two levels. The computational volume defined previously will hereby be referred to as the fine resolution case; the first level below this will be referred to as the medium resolution; and the 2nd level, whose cell sizes are exactly double that of the fine resolution case, will be referred to as the coarse resolution.

Aerodynamic loading results for all three resolutions are shown in Table 1. Since the aerodynamic thrust results were underpredicted by approximately 17%, the surface pressures at two different spanwise sections, 0.50R and 0.75R, were extracted from the simulation and compared to results generated using both the open-source software, XFOIL, and FUN3D (Ref. 19).

The total lift force generated using the FUN3D simulation was within 3% of the experimental value at 0.75R. Because of this, the angle of attack used to generate the surface pressure distributions in XFOIL was varied until pressure suction

Table 2: Sectional Spanwise Aerodynamic Loading Results.

(a) Aerodynamic Loading Results at 0.50R.

Source	Lift	Relative Error
XFOIL	0.2729 lb	
FUN3D	0.2862 lb	4.86%
PowerFLOW	0.2342 lb	14.19%

(b) Aerodynamic Loading Results at 0.75R.

Source	Lift	Relative Error
XFOIL	0.6163 lb	
FUN3D	0.6460 lb	2.31%
PowerFLOW	0.5174 lb	19.91%

peaks of the XFOIL and FUN3D results matched (Fig. 5). The heuristically determined angles of attack at the 0.50R and 0.75R spanwise sections were respectively 2 degrees and 0.6 degrees lower than those calculated using Blade Element Theory (BET), signifying an overprediction of induced velocity from the PowerFLOW simulation. The surface pressure distributions at these two spanwise locations for all three simulations were then integrated to produce lift force estimates and relative error percentages (Table 2). This increase in induced velocity is intrinsic to the PowerFLOW simulation and may very well explain the underprediction in the thrust generated by the rotor.

AEROACOUSTIC RESULTS

Acoustic Data Post-Processing

Techniques similar to those of Refs. 1 and 5 were used to post-process the acoustic pressure time histories from both the simulation and the experiment to differentiate between the periodic (tonal) and stochastic (broadband) noise contributions of each data set. This section discusses how the signal differentiation process was applied to the computational data sets. The reader is referred to Ref. 5 for specific processing details pertaining to the experimental data.

First, the acoustic pressure time history was separated into six equally sized bins correspondent to the six rotor revolutions of recorded data. These six revolutions were averaged together to obtain a mean rotor revolution, which served as the basis for the subsequent tonal noise calculations. This mean rotor revolution was then subtracted from each of the six bins of raw acoustic pressure time history data to obtain the residual acoustic pressure time history, or broadband noise component. The mean rotor revolution was repeated enough times to attain a 10 Hz frequency resolution, which was then processed by treating the repeated rotor revolution as an aperiodic signal, computing the Fast Fourier Transform (FFT) of the data, then using Equation 1 to produce a narrowband spectrum of the sound pressure level (SPL) for a direct comparison to the broadband noise.

$$\mathrm{SPL} = 10\log_{10}\left(\frac{P_{xx} * \Delta \mathrm{f}}{p_{\mathrm{ref}}^2}\right) \tag{1}$$

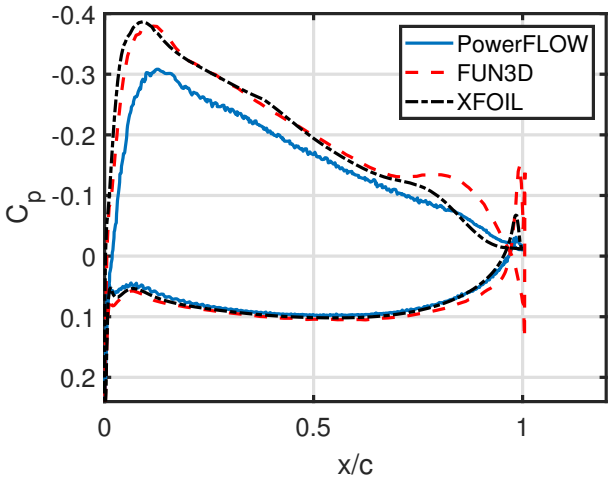

(a) Pressure Distribution at 0.5R.

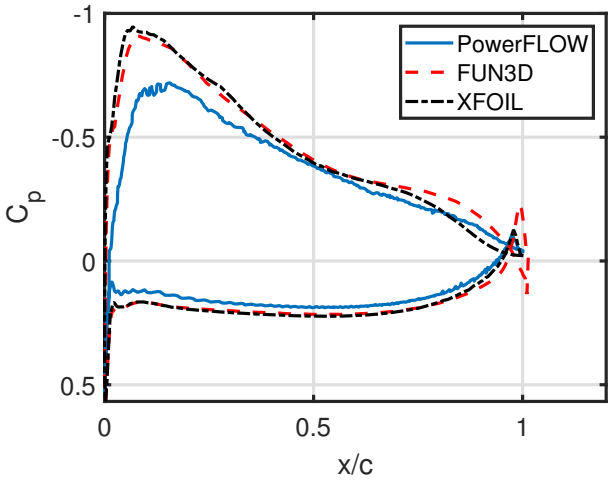

(b) Pressure Distribution at 0.75R.

Figure 5: Spanwise Pressure Distribution Comparison.

Another post-processing technique was used that filtered the raw acoustic pressure time history using a 2nd-order Butterworth narrowband pass filter with a ± 30 Hz frequency band centered at the first 10 shaft harmonics. This filter served the purpose of mitigating spectral leakage associated with different measurement and post-processing techniques. This effectively confined all energy associated with each shaft harmonic to the frequency value of the harmonic itself, allowing for a better comparison between the spectral data of the simulation to that of the experiment. The root mean square (RMS) value of this filtered data was used to calculate the acoustic SPL amplitudes of each shaft harmonic using Equation 2.

$$\mathrm{SPL}_{n*SH} = 20\log_{10}\left(\frac{\bar{p}_{\mathrm{rms}}}{p_{\mathrm{ref}}}\right) \tag{2}$$

The residual (broadband) acoustic pressures were also treated as aperiodic signals of which the FFT was calculated. The SPL and power spectral density (PSD) of these processed signals were then calculated using Equations 1 and 3, the former

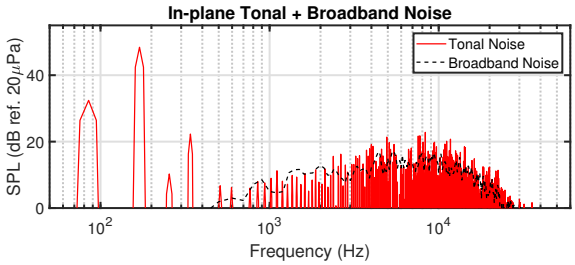

(a) In-plane at 16R, $\theta = 0°$.

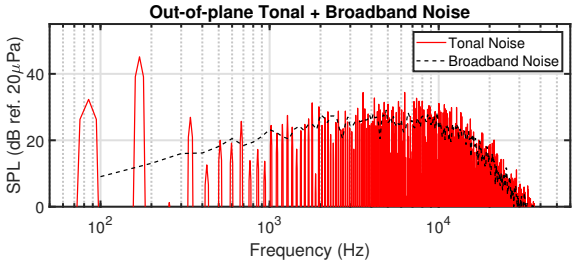

(b) Out-of-plane at 16R, $\theta = -45°$.

Figure 6: Acoustic Narrowband Spectra of Tonal and Broadband Noise at Different Observer Locations.

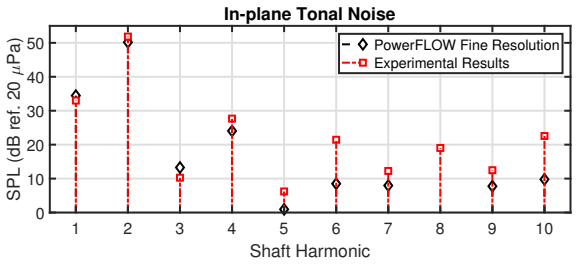

(a) In-plane at 16R, $\theta = 0°$.

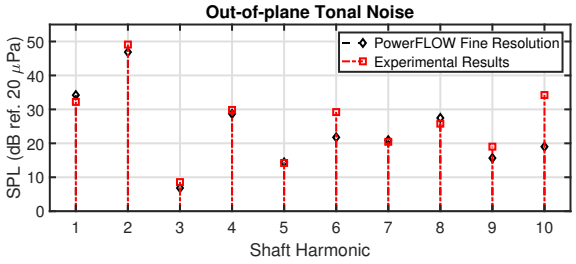

(b) Out-of-plane at 16R, $\theta = -45°$.

Figure 7: Shaft Harmonics at Different Observer Locations.

of which used a frequency resolution of 100 Hz due to the limited number of rotor revolutions of data. SPL data were then used to calculate one-third octave band SPL values ($SPL_{1/3}$), as well as scaled to the 10 Hz resolution of the tonal noise contribution for a 1-to-1 comparison between the two.

$$\text{PSD} = 10\log_{10}\left(\frac{P_{xx}}{p_{\text{ref}}^2}\right) \tag{3}$$

These post-processing techniques were used on the acoustic pressures propagated to two observer locations, both of which were in front of the rotor at a radial distance of 16R away. One observer was in plane with the rotor and the other was -45 degrees below. The narrowband SPL spectra for both the in-plane and out-of-plane observers are shown in Fig. 6 for clarity, as well as to serve as a basis for comparison between the tonal and broadband noise.

Although the BPF amplitudes dominate at the lower frequencies, these are less perceptible to human audibility when compared to the 1 kHz to 10 kHz range. The results in Fig. 6 show that, in the context of sUAS vehicles, broadband noise is a key component to the total noise generated, especially when compared with a much more heavily loaded, full-sized, conventional helicopter rotor.

Tonal Noise Comparison

The acoustic amplitudes of the first 10 shaft harmonics for both the in-plane and out-of-plane observers are plotted in Fig. 7. The shaft harmonics were chosen specifically to elucidate any potential differences in geometry between the CAD model and the physical rotor. It can be ascertained by the first shaft harmonic, shown in Fig. 7, that there are geometric blade to blade inconsistencies; however, this plot provides further proof that the CAD geometry very closely resembles the physical geometry.

The second and fourth shaft harmonics correspond to the first and second blade passage frequencies (BPFs) and show good comparison between the simulation and the experiment. Since the simulation underpredicted the aerodynamic loading, it was expected that these two shaft harmonics would be slightly underpredicted.

Directivity plots of the first and second BPF amplitudes were also generated in Fig. 8 along an arc located 16R away from the rotor using the same BPF filtering technique discussed previously and are plotted against both experimental results and results generated using ANOPP's Propeller Analysis System (PAS) (Ref. 20). The in-plane location is designated as 0 degrees, with 16R above the rotor being the positive 90 degree location and 16R below the rotor, the negative 90 degrees location. The first BPF prediction is seen to trend fairly well with only a few dB underprediction for both the PowerFLOW and the PAS predictions. The second BPF, however, is completely missed by both predictions with the PowerFLOW prediction being only a few dB off for locations in and below the plane of the rotor. This predicted trend is seen to match that of a very similar rotor noise prediction in Ref. 5.

Broadband Noise Comparison

Comparisons between simulations and experimental results of PSD and $SPL_{1/3}$ are shown for both the in-plane and out-of-plane observers in Figs. 9 & 10, respectively. As shown in these figures, simulation results from the fine grid resolution compare well with the experimental results between 1 kHz and 10 kHz. This proves that, although the simulation used turbulence modeling coupled with wall functions to calculate part of the boundary layer, the unsteady pressure fluctuations caused by the energetic turbulence in the outer region of the

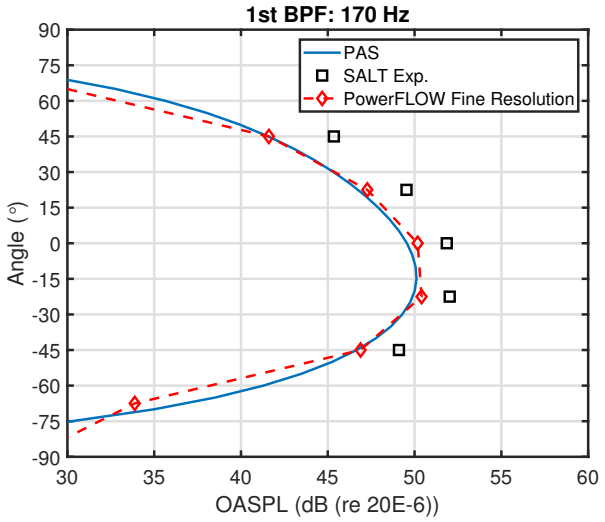

(a) Directivity of 1*BPF.

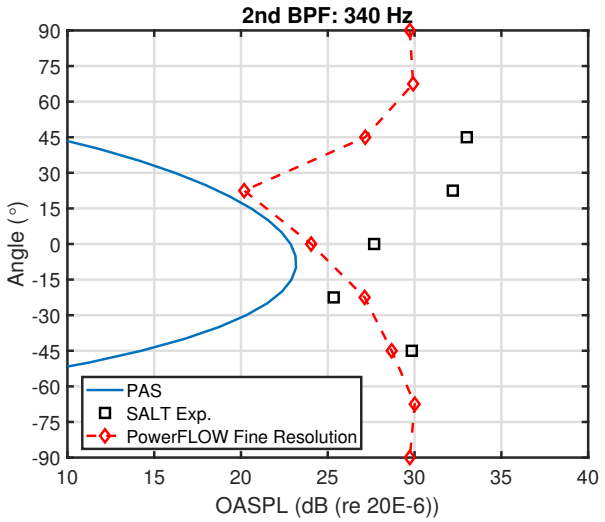

(b) Directivity of 2*BPF.

Figure 8: Directivity Plots of First and Second BPFs at 16R.

boundary layer as well as the pressure scattering on the trailing edge of the rotor from turbulence in the near wake was simulated accurately.

The discrepancy in lower frequency broadband noise below 1.5 kHz is thought to be attributed to TIN (Refs. 21 and 22). For this hover simulation, the farfield boundaries of the computational domain were prescribed to a zero velocity condition, meaning that any atmospheric turbulence associated with the simulation will be generated by the rotor. Because of this, the true location of the initial turbulent structure formations may lack the spatial resolution required to adequately capture them, meaning that their starting point may differ from the physical experiment. This would imply that any induced turbulence in the simulation would be underpredicted, which could explain the discrepancy below 1.5 kHz. The error in frequencies above 10 kHz will be explained in the Grid Sensitivity section.

The broadband noise directivity was also calculated using the

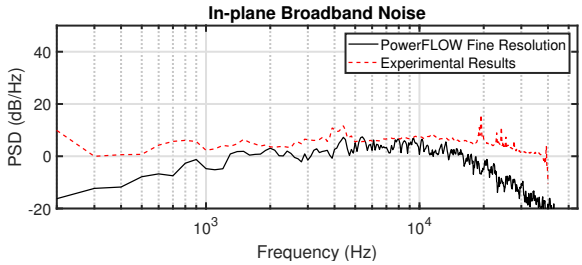

(a) In-plane at 16R, $\theta = 0°$.

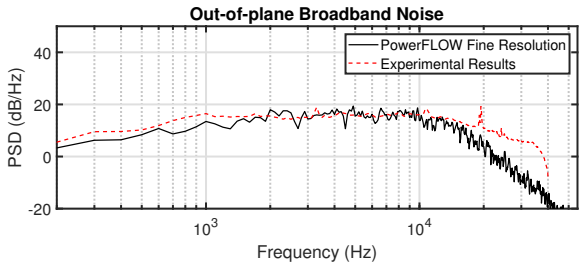

(b) Out-of-plane at 16R, $\theta = -45°$.

Figure 9: Broadband Noise Autospectra at Different Observer Locations.

same aforementioned filtering process. The residual acoustic pressure time history was filtered over frequencies between 500 Hz and 10 kHz, and has been plotted against experimental results in Fig. 11. The predicted directivity very closely approximates the experimental results with an underprediction of only a few dB at the in-plane observer location, which was also shown in Figs. 9a and 10a.

Grid Sensitivity

Since the focal point of this research was broadband noise prediction, the PSDs of broadband noise from the three grid resolutions discussed previously were calculated and plotted against each other on both a logarithmic and linear basis in Fig. 12 to discern any trends. The broadband noise contribution presents itself as a loading noise source in the context of an impermeable FW-H surface formulation and behaves as a dipole. Because of this, the out-of-plane observer location was thought to be the best observer location for this grid comparison; therefore results at the in-plane observer will not be shown.

It can be seen that although the aerodynamic thrust from the medium resolution case differed from the fine resolution case by about 4%, the broadband noise predictions from both of these resolutions trend very well up to a frequency of around 11 kHz. This suggests that even the medium resolution case maintained enough spatial refinement to resolve most of the broadband noise; however, both the medium and coarse cases are seen to roll off sooner than the fine case due to their decreased spatial resolution, which explains the aforementioned discrepancy between the simulation and experimental results at frequencies above 10 kHz. This trend is further exemplified on a linear basis in Fig. 12b. The grid resolution could be increased to capture some of this higher energy content but

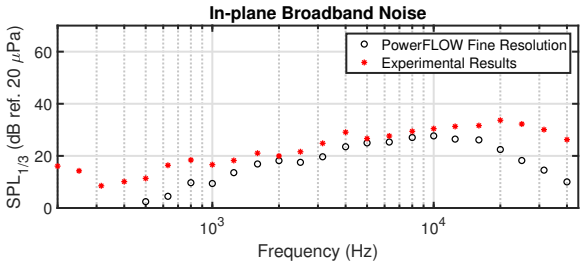

(a) In-plane at 16R, $\theta = 0°$.

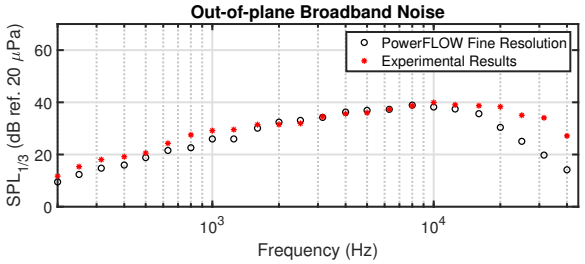

(b) Out-of-plane at 16R, $\theta = -45°$.

Figure 10: Broadband Noise Spectra at Different Observer Locations.

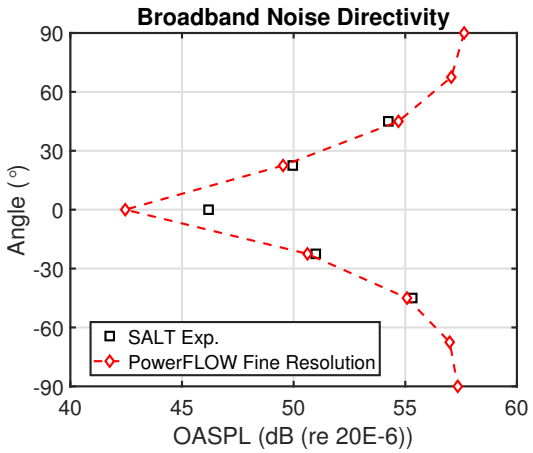

Figure 11: Broadband Noise Directivity Plot at 16R.

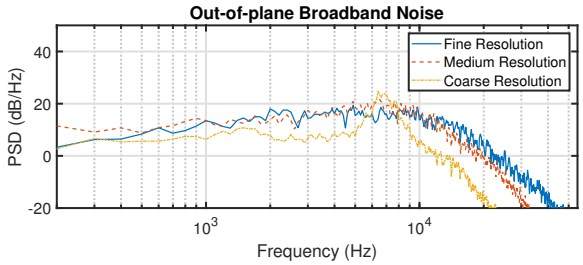

(a) Broadband Noise Autospectra on a Logarithmic Basis.

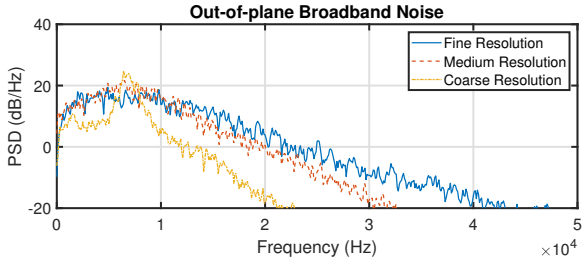

(b) Broadband Noise Autospectra on a Linear Basis.

Figure 12: Broadband Noise Autospectra, Out-of-plane at 16R, $\theta = -45°$.

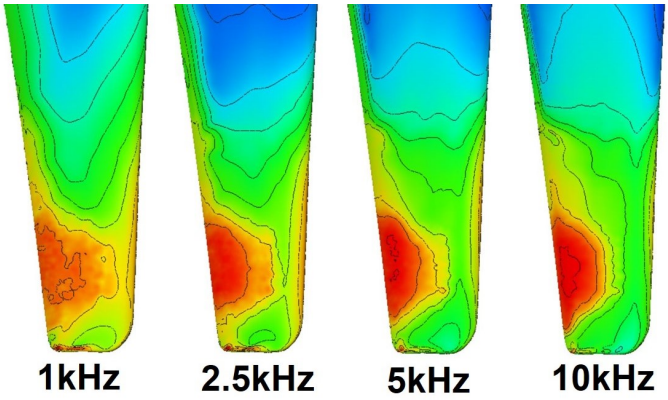

Figure 13: $SPL_{1/3}$ of On-surface Pressure Perturbations. Range: 64dB - 130dB.

would be impractical due to the increased computation time. The human ear is less sensitive to noises above 10 kHz, as seen by an A-weighting curve. Therefore, it is less important to be able to resolve these frequencies, at least in the context of full scale sUAS vehicles.

The coarse resolution case lacked the spatial refinement to adequately capture any of the broadband noise, which explains the peak around 7 kHz in Fig. 12. It appears that the energy from these higher, underresolved frequencies was grouped together under the highest resolvable frequency.

Aeroacoustic Sources

It was thought to investigate the broadband noise sources in more detail. Therefore, $SPL_{1/3}$ values of the unsteady pressure perturbations on the suction side of the rotor blade were calculated, similarly to what was done in Ref. 13. This is shown in Fig. 13 for frequencies ranging between 1 kHz and 10 kHz. It should be noted that these pressure perturbations are in source time and technically are not acoustic pressures. Still, they provide valuable insight to acoustic source identification.

It can be seen in Fig. 13 that almost all of the noise was generated by the pressure scattering of near wake turbulence on the trailing edge with the tip vortex formation having a contribution at frequencies below 5kHz. Both of these noise generating mechanisms are categorized under broadband self-noise, with the former being known as turbulent boundary layer trailing edge noise and the latter being tip vortex formation noise (Ref. 2).

BWI noise, or noise caused by a perpendicular blade vortex interaction, was thought to have a negligible contribution, shown by the broad area over the leading edge with minuscule $SPL_{1/3}$ values. This broad, affected area is, however, indicative of some form of leading edge noise, especially at

the lower frequency range, which was thought to be TIN. It was thought that the high rotor rotational rate, in conjunction with the twist and camber of the rotor blades, were such that these blade tip vortices were convected downward at a high enough rate as to not produce any significant interactional effects. The miss distance between the center of the vortex core of the perpendicular blade vortex and the leading edge of the blade was calculated to be $1.04c_{0.75}$, which is further proof of the negligible BWI effects when comparing to Ref. 23.

CONCLUSIONS AND FUTURE WORK

In this work, an LBM-VLES was employed using the commercial software, PowerFLOW, to simulate the flowfield encompassing a representative sUAS rotor, the DJI-9450, in a static hover condition over three computational grids of varying resolution. The finest of these grids consisted of 565 million hexahedron voxels, or 133 million fine equivalent voxels. The DJI-9450 geometry was taken from the GrabCAD community website and validated at different spanwise locations by comparing to measurements provided in Ref. 18.

The three grid resolutions were used to predict both aerodynamic and aeroacoustic results, which were compared to experimental results acquired in the SALT anechoic chamber facility at the NASA Langley Research Center (Ref. 9). The total predicted aerodynamic thrust generated by the rotor underpredicted the experimental results for all three grid resolutions, with the finest resolution being underpredicted by approximately 17%. Pressure distributions were extracted from the fine resolution case at discrete spanwise locations and compared with predictions generated via lower fidelity prediction methods, which showed an overprediction of induced velocity associated with the PowerFLOW prediction.

The rotor was treated as an impermeable FW-H surface and a forward-time solution (Ref. 7) of Farassat's formulation 1A (Ref. 8) was used to propagate acoustic pressures from the rotor surface to defined observer locations within the post-processing software suite, PowerACOUSTICS. The methodology for processing this acoustic time pressure history was discussed before total acoustic spectra were shown for observers located at 16R away in the plane of the rotor as well as -45 degrees below the rotor. These spectra showed broadband noise to be a dominant noise source in the 1 kHz to 10 kHz range. Tonal shaft harmonic amplitudes were also calculated, which further validated the accuracy of the modeled rotor geometry. These results also showed favorable comparison for the first and second BPF amplitudes with a slight underprediction, as expected based upon aerodynamic loading results.

Directivities of the first and second BPF amplitudes were also shown for an arc located 16R away from the rotor, which trended well with the experimental results and predicted results from ANOPP-PAS (Ref. 20) for the first BPF. The second BPF showed a discrepancy in the predictions from both PAS and PowerFLOW, which is thought to be attributed to the out of phase behavior of the thickness and loading noise.

Broadband noise predictions were also compared against experimental results on both a PSD and $SPL_{1/3}$ basis, which showed favorable agreement, with a slight discrepancy in frequencies below 1.5 kHz being attributed to an underprediction in the rotor induced turbulence. The roll off at frequencies above 11 kHz was shown to be dependent upon the spatial resolution of the computational domain, with the coarsest resolution of the three grids lacking the proper refinement to resolve any of the broadband noise.

Aeroacoustic noise sources were interrogated in further detail by calculating $SPL_{1/3}$ values of the unsteady pressure perturbations on the suction side of the rotor blade at discrete frequencies between 1 kHz and 10 kHz, which were shown in Fig. 13. It was seen that broadband self-noise was the most prominent noise source, with the majority of this self-noise being due to turbulent boundary layer trailing edge noise caused by pressure scattering of near wake turbulence on the trailing edge focused over the outboard portion of the blade. Tip vortex formation noise was also seen to have a contribution at frequencies below 5 kHz. BWI noise was not seen to make any significant contribution to the total noise, shown by the negligible $SPL_{1/3}$ values on the leading edge and by comparing the calculated blade vortex miss distance of $1.04c_{0.75}$ to values from Ref. 23.

The results from this study conclude that the high fidelity LBM-VLES method predicts both the tonal and broadband noise emanating from this particular rotor well, however, with drastic underprediction of aerodynamic forces and at a high computational cost. Work is currently being done to investigate the applicability of this prediction method to different rotors, as well as to develop tools for further elucidation of acoustic noise sources in observer time, as opposed to the source time approach used in the context of this work. With the increasing demand of these sUAS vehicles, the high turnaround rates associated with lower fidelity prediction methodologies will be vital to acoustic optimization procedures. Further work is necessary to abate discrepancies from these lower fidelity predictions methods, specifically for the broadband noise associated with TIN and interactional aerodynamic effects such as BWI.

Author contact: Christopher S. Thurman,
christopher.thurman@nasa.gov

ACKNOWLEDGMENTS

The authors would like to thank David Lockard of the Computational Aerosciences Branch at NASA Langley Research Center for his unwavering assistance with the PowerFLOW software suite, as well as with allocating computational resources that were vital to performing the simulations. The authors would also like to thank Damiano Casalino and Wouter van der Velden from Dassault Systémes for their diligent support and expertise. This work was funded by the NASA Revolutionary Vertical Lift Technology (RVLT) project.

REFERENCES

1. Zawodny, N. S. and Pettingill, N. A., "Acoustic Wind Tunnel Measurements of a Quadcopter in Hover and

Forward Flight Conditions," 47th International Congress and Exposition on Noise Control Engineering, Chicago, IL, Aug. 2018.

2. Brooks, T. F., Pope, D. S., and Marcolini, M. A., *Airfoil Self-Noise and Prediction,* Hampton, VA, NASA RP 1218, 1989.

3. Brooks, T. F. and Burley, C. L., "Blade Wake Interaction Noise for a Main Rotor," *Journal of the American Helicopter Society,* Vol. 49, (1), 2004, pp. 11-27.
doi: 10.4050/JAHS.49.11

4. Burley, C. L. and Brooks, T. F., "Rotor Broadband Noise Prediction with Comparison to Model Data," *Journal of the American Helicopter Society,* Vol. 49, (1), 2004, pp.28-42.
doi: 10.4050/JAHS.49.28

5. Zawodny, N. S., Boyd Jr., D. D., and Burley, C. L., "Acoustic Characterization and Prediction of Representative, Small-Scale Rotary-Wing Unmanned Aircraft System Components," AHS International 72nd Annual Forum, West Palm Beach, FL, May 2016.

6. Casalino, D., van der Velden, W.C.P., and Romani, G., "Community Noise of Urban Air Transportation Vehicles," *AIAA Paper 2019-1834,* 2019.

7. Casalino, D., "An Advanced Time Approach for Acoustic Analogy Predictions," *Journal of Sound and Vibration,* vol. 261, no. 4, pp. 583-612, 2003.

8. Farassat, F., *Derivation of Formulations 1 and 1A of Farassat,* Hampton, VA, NASA TM 2007-214853, 2007.

9. Grosveld, F. W., "Calibration of the Structural Acoustics Loads and Transmission Facility at NASA Langley Research Center," InterNoise 99, 1999.
doi: 10.1142/S0129183198001060

10. Avallone, F., Casalino, D., and Ragni, D., "Impingement of a Propeller-slipstream on a Leading Edge with a Flow-permeable Insert: A Computational Aeroacoustic Study," *International Journal of Aeroacoustics,* vol. 17, iss. 6-8, 2018, pp. 687-711.
doi: 10.1177/1475472X18788961

11. Gonzalez-Martino, I., Wang, J., Romani, G., and Casalino, D., "Rotor Noise Generation in a Turbulent Wake using Lattice-Boltzmann Methods," 24th AIAA/CEAS Aeroacoustics Conference, Atlanta, GA, June 2018.
doi: 10.2514/6.2018-3477

12. Casalino, D., van der Velden, W.C.P., and Romani, G., "Aeroacoustic Analysis of Urban Air Operations using the LB/VLES Method," 25th AIAA/CEAS Aeroacoustics Conference, Delft, The Netherlands, May 2019.

13. Nardari, C., Casalino, D., Polidoro, F., Coralic, V., Brodie, J., and Lew, P., "Numerical and Experimental Investigation of Flow Confinement Effects in UAV Rotor Noise," 25th AIAA/CEAS Aeroacoustics Conference, Delft, The Netherlands, May 2019.

14. Bhatnagar, P., Gross, E., and Krook, M., "A Model for Collision Processes in Gases. I. Small Amplitude Processes in Charged and Neutral One-Component Systems," *Phys. Rev.,* vol. 94, iss. 3, 1954, pp. 511-525.

15. Succi, S., *The Lattice Boltzmann Equation for Fluid Dynamics and Beyond,* 1st ed., Clarendon Press, Oxford, 2001.

16. Shan, X., Yuan, X.-F., and Chen, H., "Kinetic Theory Representation of Hydrodynamics: a Way Beyond the Navier-Stokes Equation," *Journal of Fluid Mechanics,* vol. 550, 2006, pp. 413-441.
doi: 10.1017/S0022112005008153

17. Teixeira, C., "Incorporating Turbulence Models into the Lattice-Boltzmann Method," *International Journal of Modern Physics C,* vol. 9, no. 8, 1998, pp. 1159-1175.

18. Russell, C., Willink. G., Theodore, C., Jung, J., and Glasner, B., *Wind Tunnel and Hover Performance Test Results for Multicopter UAS Vehicles,* Moffett Field, CA, NASA TM 2018-219758, 2018.

19. "FUN3D User Manual," http://fun3d.larc.nasa.gov.

20. Nguyen, L. C. and Kelly, J. J., "A Users Guide for the NASA ANOPP Propeller Analysis System," Hampton, VA, NASA CR 4768, 1997.

21. Amiet, R. K., "Noise Produced by Turbulent Flow into a Rotor: Theory Manual for Noise Calculation," Hampton, VA, NASA Contractor Report 181788, June 1989.

22. Amiet, R. K., "Noise Produced by Turbulent Flow into a Propeller or Helicopter Rotor," *AIAA Journal,* vol. 15, no. 3, 1997, pp. 307-308.

23. Wittmer, K. S., Devenport, W. J., and Glegg, S. A. L., "Effects of Perpendicular Blade-Vortex Interaction, Part 2: Parameter Study," *AIAA Journal,* vol. 37, no. 7, 1999, pp. 813-817.
doi: 10.2514/2.7528